

YITP-19-124

$\Lambda\Lambda$ and $N\Xi$ interactions from Lattice QCD near the physical point

Kenji Sasaki^{a,b}, Sinya Aoki^{a,b,c}, Takumi Doi^{b,d}, Shinya Gongyo^b, Tetsuo Hatsuda^{d,b},
Yoichi Ikeda^{e,b}, Takashi Inoue^{f,b}, Takumi Iritani^b, Noriyoshi Ishii^{e,b}, Keiko Murano^{e,b},
Takaya Miyamoto^b, (HAL QCD Collaboration)

^a*Center for Gravitational Physics, Yukawa Institute for Theoretical Physics, Kyoto University, Kyoto 606-8502, Japan*

^b*Quantum Hadron Physics Laboratory, RIKEN Nishina Center, Saitama 351-0198, Japan*

^c*Center for Computational Sciences, University of Tsukuba, Tsukuba 305-8577, Japan*

^d*RIKEN Interdisciplinary Theoretical and Mathematical Sciences Program (iTHEMS), Saitama 351-0198, Japan*

^e*Research Center for Nuclear Physics (RCNP), Osaka University, Osaka 567-0047, Japan*

^f*Nihon University, College of Bioresource Sciences, Kanagawa 252-0880, Japan*

Abstract

The S -wave $\Lambda\Lambda$ and $N\Xi$ interactions are studied on the basis of the (2+1)-flavor lattice QCD simulations close to the physical point ($m_\pi \simeq 146\text{MeV}$ and $m_K \simeq 525\text{MeV}$). Lattice QCD potentials in four different spin-isospin channels are extracted by using the coupled-channel HAL QCD method and are parametrized by analytic functions to calculate the scattering phase shifts. The $\Lambda\Lambda$ interaction at low energies shows only a weak attraction, which does not provide a bound or resonant dihyperon. The $N\Xi$ interaction in the spin-singlet and isospin-singlet channel is most attractive and lead the $N\Xi$ system near unitarity. Relevance to the strangeness=-2 hypernuclei as well as to two-baryon correlations in proton-proton, proton-nucleus and nucleus-nucleus collisions is also discussed.

Keywords: Hyperon interaction, Lattice QCD, H-dibaryon

Email address: kenjis@yukawa.kyoto-u.ac.jp (Kenji Sasaki)
Preprint submitted to Journal of LATEX Templates

1. Introduction

The baryon-baryon interactions in the strangeness $\mathcal{S} = -2$ sector attract much attention to understand the nature of the dihyperon [1, 2, 3], the structures of double- Λ or Ξ hypernuclei [4, 5, 6], and the two-particle correlations in pp, pA and AA collisions [7, 8, 9]. Although various models with phenomenological parameters have been proposed so far for the hyperon interactions, it is of crucial importance at present to derive the $\mathcal{S} = -2$ interaction from first principle lattice QCD simulations. Such an attempt became possible by the development of high performance computing facilities as well as the theoretical progress of the HAL QCD method [10, 11, 12].

In this paper, we report the (2+1)-flavor lattice QCD results of the low-energy scattering of $N\Xi$ and $\Lambda\Lambda$ systems at nearly physical point ($m_\pi \simeq 146$ MeV and $m_K \simeq 525$ MeV) with a large spacetime volume ($L \simeq 8.1\text{fm}$) on the basis of the coupled-channel HAL QCD method [13, 14, 15]. We note that the results for the $N\Omega$ ($\mathcal{S} = -3$) system [16] and $\Omega\Omega$ ($\mathcal{S} = -6$) system [17] have been recently reported with the same lattice setup.

The organization of this paper is as follows. In Sec. 2, we briefly review the coupled-channel HAL QCD method. In Sec. 3, our setup of lattice QCD simulations is summarized. In Sec. 4, numerical results of the $\Lambda\Lambda$ and $N\Xi$ potentials are presented. After fitting the numerical data of the lattice QCD potentials by analytic functions in Sec. 5, we discuss the scattering observables such as the scattering phase shifts and inelasticity in Sec. 6. Sec. 7 is devoted to summary and concluding remarks.

2. Coupled-channel baryon-baryon interaction

In the coupled-channel HAL QCD method [13, 14, 15], baryon-baryon interactions are expressed by an energy independent potential $U_{c'}^c(\vec{r}, \vec{r}')$, which reproduces the scattering phase shifts subject to the QCD Lagrangian. Here the channel c (c') denotes the system of two particles c_1 and c_2 (c'_1 and c'_2) with the rest masses m_{c_1} and m_{c_2} ($m_{c'_1}$ and $m_{c'_2}$), respectively. Let us start with a function R_d^c which is defined as a normalized four-point correlation between channels c and d ;

$$\begin{aligned} R_d^c(\vec{r}, t) &\equiv \frac{\sum_{\vec{x} \in V} \langle 0 | B_{c_1}(\vec{r} + \vec{x}, t) B_{c_2}(\vec{x}, t) \overline{\mathcal{J}}_d(0) | 0 \rangle}{\sqrt{Z_{c_1}} \sqrt{Z_{c_2}} \exp[-(m_{c_1} + m_{c_2})t]} \\ &= \sum_j \psi_{W_j}^c(\vec{r}) e^{-\Delta W_j^c t} A_d^{W_j} + \dots, \end{aligned} \quad (1)$$

where B_{c_1} and B_{c_2} are local interpolating operators for the baryons, while $\mathcal{J}_d(0)$ is a source operator of two baryons at $t = 0$. The wave function renormalization factors for single baryons are denoted by Z_{c_1} and Z_{c_2} . The j -th eigen energy of the total system is denoted by W_j , while the energy shift from the threshold of the channel c is defined by $\Delta W_j^c = W_j - (m_{c_1} + m_{c_2})$. The overlap factor of the source operator to the j -th eigen state is given by $A_d^{W_j} = \langle W_j | \overline{\mathcal{J}}_d(0) | 0 \rangle$. The Nambu-Bethe-Salpeter (NBS) wave function with total energy W_j in the channel c is denoted by $\psi_{W_j}^c(\vec{r})$. The ellipses in Eq. (1) corresponds to the inelastic contributions beyond the elastic scatterings in the coupled channel space.

An energy-independent non-local potential can be defined through the partial differential equation satisfied by $R_d^c(\vec{r}, t)$ (see [15] for details):

$$\left(\frac{1 + 3\delta_c^2}{8\mu_c} \frac{\partial^2}{\partial t^2} - \frac{\partial}{\partial t} + \frac{\nabla^2}{2\mu_c} \right) R_d^c(\vec{r}, t) = \sum_{c'} \int d^3r' U_{c'}^c(\vec{r}, \vec{r}') \Delta_{c'}^c R_d^{c'}(\vec{r}', t), \quad (2)$$

where $\mu_c = m_{c_1} m_{c_2} / (m_{c_1} + m_{c_2})$ and $\delta_c \equiv (m_{c_1} - m_{c_2}) / (m_{c_1} + m_{c_2})$. The factor $\Delta_{c'}^c \equiv \exp[-(m_{c'_1} + m_{c'_2} - m_{c_1} - m_{c_2})t]$ plays a role to compensate the threshold energy difference between channels c and c' . We note that the term with second-order time-derivatives in Eq. (2) represents the relativistic effect. The terms with higher-order time-derivatives are neglected, since those contributions are numerically negligible. The NBS wave functions $\psi_{W_j}^c(\vec{r})$ are in general not orthogonal to each other, so that the potential matrix $U_{c'}^c(\vec{r}, \vec{r}')$ is not necessarily Hermitian. Nevertheless, the energy eigenvalues W_j are real by construction.

In the $\mathcal{S} = -2$ channel for the octet baryons, there are four asymptotic states from below, $\Lambda\Lambda$, $N\Xi$, $\Lambda\Sigma$ and $\Sigma\Sigma$. We consider only the two low-lying scattering states throughout this paper, so that we have two-by-two potential $U_{c'}^c(\vec{r}, \vec{r}')$ with c and c' being either $\Lambda\Lambda$ or $N\Xi$. All the inelastic effects outside of this two-by-two coupled channel space are included implicitly in $U_{c'}^c$ as long as W_j stays below the $\Lambda\Sigma$ threshold [13, 14].

We use the following local interpolating operator for octet baryons,

$$B(x) = \epsilon^{\alpha\beta\gamma} (q_{1,\alpha}^T(x) C \gamma_5 q_{2,\beta}(x)) q_{3,\gamma}(x) \equiv [q_1 q_2] q_3, \quad (3)$$

where α , β and γ are color indices, and q_1 , q_2 and q_3 takes either u , d or s . Then the interpolating operators relevant to our analysis are $B_\Lambda(x) = ([sd]u + [us]d - 2[du]s)/\sqrt{6}$, $B_p(x) = [ud]u$, $B_n(x) = [ud]d$, $B_{\Xi^0}(x) = [su]s$ and $B_{\Xi^-}(x) = [sd]s$. The source operator $\mathcal{J}_d(0)$ is defined by the product of the baryon operator Eq. (3) with $q_i(x)$ replaced by $Q_i(0) = \sum_{\vec{x}} q_i(\vec{x}, 0)$ i.e. $\mathcal{J}_d = ([Q_1 Q_2] Q_3)_{d_1} ([Q_{1'} Q_{2'}] Q_{3'})_{d_2}$ [15]. Such a wall source is known to have a large overlap with low-lying states [18, 19].

In order to handle the non-locality of the potential in Eq. (2), we employ the derivative expansion scheme [11, 14];

$$U_{c'}^c(\vec{r}, \vec{r}') = \left(V_{c'}^c(\vec{r}) + \sum_{n=1}^{\infty} V_{c'}^{c(n)}(\vec{r}) \nabla^n + \dots \right) \delta(\vec{r} - \vec{r}'). \quad (4)$$

In this work we consider only the leading order potential, $V_{c'}^c(\vec{r})$: The validity of such truncation at low energies can be checked by the t -dependence of the resultant potentials. See also Ref. [18] for an explicit construction of the higher order terms as well as the convergence test of the derivative expansion.

3. Simulation setup of (2+1)-flavor QCD

Lattice QCD simulations with the lattice spacing a are performed on gauge configurations in the large volume $((L/a)^4 = 96^4)$, generated in the (2+1)-flavor lattice QCD with the Iwasaki gauge action at $\beta = 1.82$ and the non-perturbatively $\mathcal{O}(a)$ -improved Wilson quark action, together with the stout smearing, at nearly physical quark masses [20] corresponding to $m_\pi \simeq 146\text{MeV}$ and $m_K \simeq 525\text{MeV}$. The lattice

Table 1: Baryon masses m_B are given in lattice unit and GeV unit. Statistical and systematic errors are shown in the first and second parentheses, respectively. The systematic errors are estimated by the difference between the results obtained by the fit range $[t/a]_{\min.} \leq t/a \leq [t/a]_{\max.}$ in the Table and those by the range $[t/a]_{\min.} + 2 \leq t/a \leq [t/a]_{\max.} + 2$. The third parentheses given in GeV unit correspond to errors from the uncertainty in the lattice cutoff, a^{-1} .

Baryon	mass		fit range [t/a]
	[m_B/a]	[GeV]	
N	0.40949(78)(52)	0.9553(18)(12)(74)	13 – 17
Λ	0.48856(49)(9)	1.1398(11)(2)(88)	15 – 20
Σ	0.52365(37)(64)	1.2217(9)(15)(94)	15 – 20
Ξ	0.58087(51)(3)	1.3552(12)(1)(105)	20 – 25

cutoff is $a^{-1} = 2.333(18)\text{GeV}$ ($a = 0.0846(7)\text{fm}$) [20, 21] corresponding to $L \simeq 8.1\text{fm}$ in the physical unit. This is sufficiently large to accommodate the interaction potential between two particles. For quark fields, we adopt the periodic boundary condition in the spacial direction, while the Dirichlet boundary condition in the temporal direction is imposed at $t = t_0 + 48a$ with t_0 being the source time. The latter allows us to average over the forward propagation and backward propagation in time due to time-reversal and charge conjugation symmetries. The quark propagators from the wall source with the Coulomb gauge fixing are calculated by the domain-decomposed solver [22, 23, 24, 25], and then the efficient algorithm developed in [26] is employed to calculate correlation functions. See also Ref. [27] for discussions of a computational algorithm.

By utilizing the hypercubic symmetry on the lattice (4 rotations and 96 source locations) with 414 gauge configurations, the total number of measurements becomes $414_{[\text{conf.s}]} \times 4_{[\text{rot.}]} \times 96_{[\text{src.}]}$. We use the jackknife method with 23 jackknife samples and thus the bin size of $(414/23) \times 4 \times 96$ data, to estimate the statistical errors. Table 1 gives octet baryon masses assuming a 1-state fit, which are a few % heavier than the physical values due to slightly heavier quark masses. We have checked that a 2-state fit by including the data for small t/a provides baryon masses with less than 0.4% deviation from the results of the 1-state fit.

4. Numerical results of $\Lambda\Lambda$ and $N\Xi$ potentials

To characterize the S -wave $\Lambda\Lambda$ and $N\Xi$ interactions, we use the notation ${}^{2I+1,2s+1}S_J$ where I , s , and J stand for the total isospin, the total spin, and the total angular momentum, respectively. There is a channel coupling between $\Lambda\Lambda$ and $N\Xi$ in ${}^{11}S_0$, while only $N\Xi$ contributes to the other states, ${}^{31}S_0$, ${}^{13}S_1$, and ${}^{33}S_1$. Note also that the obtained (central) potentials implicitly contain the effect of the tensor interactions in the case of ${}^{13}S_1$ and ${}^{33}S_1$ channels.

In Fig. 1, the coupled channel potentials $V_{c'}^{c,({}^{11}S_0)}(r)$ in the interval $11 \leq t/a \leq 13$ are shown. (For the diagonal part ($c = c'$), we omit the suffix c' for simplicity.) See Appendix A for the examples of wider range of t/a . Within the statistical errors, no significant t -dependence is found, which implies that the leading-order truncation of the derivative expansion is reasonable. The diagonal potentials, $V^{\Lambda\Lambda}$ and $V^{N\Xi}$ in Fig. 1 (a,d),

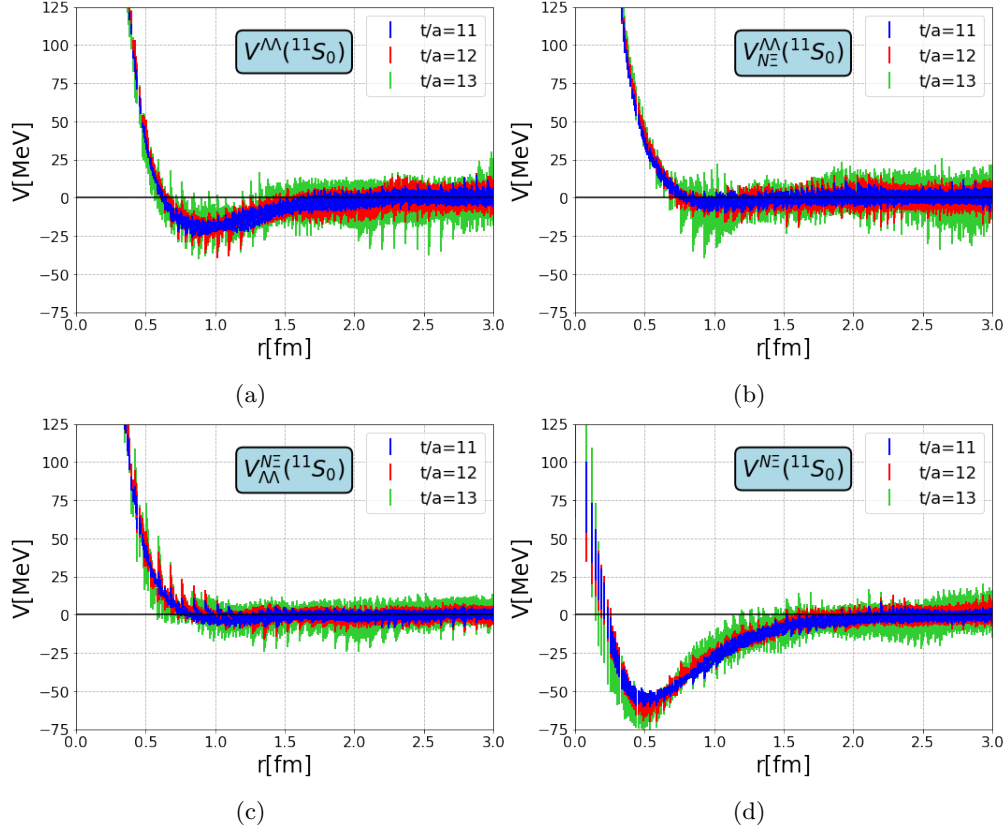


Figure 1: The S -wave coupled-channel $\Lambda\Lambda$ - $N\Xi$ potential in $^{11}S_0$. The $V^{\Lambda\Lambda}$, $V_{N\Xi}^{\Lambda\Lambda}$, $V_{\Lambda\Lambda}^{N\Xi}$ and $V^{N\Xi}$ potentials are shown in (a), (b), (c) and (d), respectively.

have attractive pocket with a long-range tail together with a short-range repulsive core. From the meson exchange picture, the one-pion exchange is allowed only in $N\Xi$ - $N\Xi$ channel. One interesting feature is that the overall attraction in $V^{N\Xi}$ is substantially larger than that in $V^{\Lambda\Lambda}$. The off-diagonal potentials shown in Fig. 1 (b,c) are found to be non-zero only at short distance, which suggests that the $\Lambda\Lambda$ - $N\Xi$ coupling is weak at low energies.

The S -wave $N\Xi$ potentials in the $^{31}S_0$, $^{13}S_1$ and $^{33}S_1$ states are shown in Fig. 2 (a), (b) and (c), respectively. Again, no significant t -dependence of the potentials is found in the interval $t/a = 11 - 13$ within the statistical errors. Also, they have stronger repulsive core and weaker mid-range attraction than those in the $^{11}S_0$ $N\Xi$ potential.

To capture the strong spin and isospin dependence of the $N\Xi$ potentials, following decomposition with the operator basis is useful [28]

$$V(r) = V_0(r) + V_\sigma(r)(\vec{\sigma}_1 \cdot \vec{\sigma}_2) + V_\tau(r)(\vec{\tau}_1 \cdot \vec{\tau}_2) + V_{\sigma\tau}(r)(\vec{\sigma}_1 \cdot \vec{\sigma}_2)(\vec{\tau}_1 \cdot \vec{\tau}_2). \quad (5)$$

This is equivalently rewritten as a relation between the spin-isospin basis and the operator

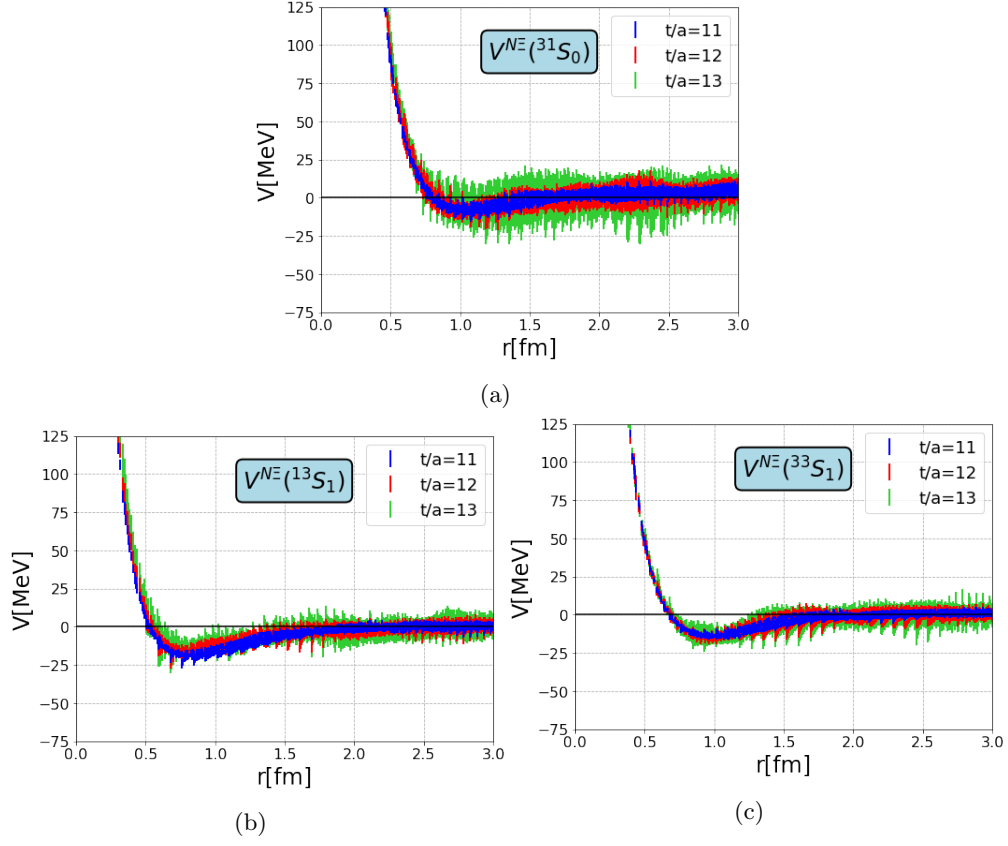


Figure 2: The S -wave $N\Xi$ potentials in $^{31}S_0$, $^{13}S_1$, $^{33}S_1$ are plotted in (a), (b) and (c), respectively.

basis;

$$\begin{pmatrix} V(^{11}S_0)(r) \\ V(^{31}S_0)(r) \\ V(^{13}S_1)(r) \\ V(^{33}S_1)(r) \end{pmatrix} = \begin{pmatrix} 1 & -3 & -3 & 9 \\ 1 & -3 & 1 & -3 \\ 1 & 1 & -3 & -3 \\ 1 & 1 & 1 & 1 \end{pmatrix} \begin{pmatrix} V_0(r) \\ V_\sigma(r) \\ V_\tau(r) \\ V_{\sigma\tau}(r) \end{pmatrix} \equiv \hat{A} \begin{pmatrix} V_0(r) \\ V_\sigma(r) \\ V_\tau(r) \\ V_{\sigma\tau}(r) \end{pmatrix}. \quad (6)$$

Shown in Fig. 3 are the $N\Xi$ potentials in the operator basis. The scalar part of the $N\Xi$ potential, $V_0^{N\Xi}$, have an attractive pocket at around 1.0 fm as well as the short-range repulsion. The former may be related to the correlated two-pion exchange as in the case of the mid-range attraction in the S -wave NN interactions. We also find that $V_{\sigma\tau}^{N\Xi}$ has a long-range attractive tail, which is consistent with the one-pion exchange picture.

5. Analytic forms of $\Lambda\Lambda$ and $N\Xi$ potentials

For phenomenological applications, it is useful to fit the LQCD potential in terms of a combination of simple analytic functions.

For the diagonal $\Lambda\Lambda$ - $\Lambda\Lambda$ potential and the off-diagonal $\Lambda\Lambda$ - $N\Xi$ potential in the $^{11}S_0$

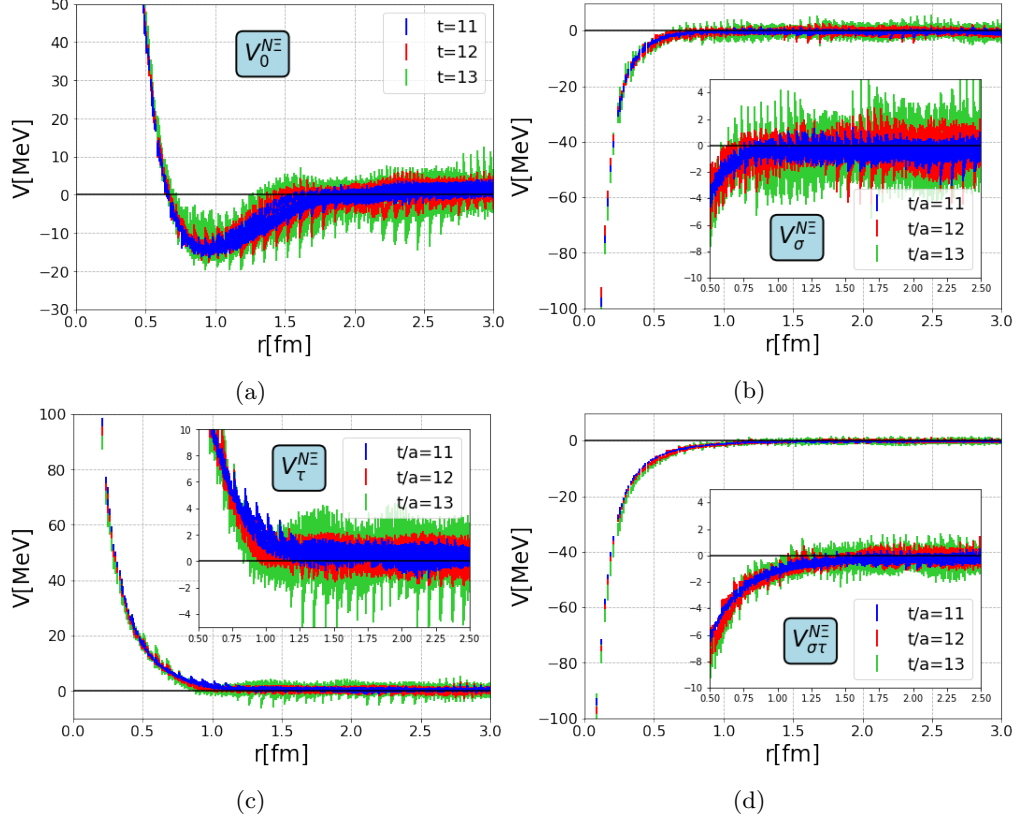


Figure 3: The S -wave $N\Xi$ potentials in the operator basis: V_0 , V_σ , V_τ and $V_{\sigma\tau}$ are shown in (a), (b), (c) and (d), respectively. The inset shows a zoom-up in the interval, $0.5 \text{ fm} \leq r \leq 2.5 \text{ fm}$.

channel shown in Fig. 1 (a,b), we consider the following fit functions,

$$V^{\Lambda\Lambda}(r) = \sum_{i=1}^2 \alpha_i^{\Lambda\Lambda} e^{-\frac{r^2}{\beta_i^{\Lambda\Lambda 2}}} + \lambda_2^{\Lambda\Lambda} [\mathcal{Y}(\rho_2^{\Lambda\Lambda}, m_\pi, r)]^2, \quad (7)$$

$$V_{N\Xi}^{\Lambda\Lambda}(r) = \sum_{i=1}^2 \alpha_i e^{-\frac{r^2}{\beta_i^2}} + \lambda_1 \mathcal{Y}(\rho_1, m_K, r), \quad (8)$$

where the Yukawa function with a form factor \mathcal{Y} is defined as

$$\mathcal{Y}(\rho, m, r) \equiv \left(1 - e^{-\frac{r^2}{\rho^2}}\right) \frac{e^{-mr}}{r}. \quad (9)$$

In Eqs. (7,8), the Gauss functions describe the short range part of the potential, while the Yukawa functions are motivated by the meson exchange picture at medium and long range distances. In particular, the squared Yukawa function in eq. (7) represents the two-pion process in the $\Lambda\Lambda - \Lambda\Lambda$ interaction whose long-range part does not exchange isospin and strangeness. Similarly, the Yukawa function in eq. (8) represents the longest range single-kaon process in the $\Lambda\Lambda - N\Xi$ transition. Note that the kaon and pion masses m_K and m_π are fixed to be the measured values on the lattice, 525 MeV and 146 MeV, respectively.

As for the fitting to the $N\Xi$ potentials in Fig. 1 (d) and Fig. 2 (a,b,c), we consider the following analytic form;

$$V(C)(r) = \sum_{i=1}^3 \alpha_i(C) e^{-\frac{r^2}{\beta_i^2}} + \lambda_2(C) [\mathcal{Y}(\rho_2, m_\pi, r)]^2 + \lambda_1(C) \mathcal{Y}(\rho_1, m_\pi, r), \quad (10)$$

with C being $^{11}S_0$, $^{31}S_0$, $^{13}S_1$ or $^{33}S_1$. The range parameters $\beta_{1,2,3}$ and $\rho_{1,2}$ for $N\Xi$ potentials are assumed to be independent of C . The above form is motivated by the following analytic forms in the operator basis where the one-pion and two-pion exchange contributions are singled out explicitly in $V_{\sigma\tau}$ and V_0 , respectively;

$$\begin{aligned} V_0(r) &= \sum_{i=1}^3 \alpha_i^{(0)} e^{-\frac{r^2}{\beta_i^2}} + \lambda_2^{(0)} [\mathcal{Y}(\rho_2, m_\pi, r)]^2 \\ V_\sigma(r) &= \sum_{i=1}^3 \alpha_i^{(\sigma)} e^{-\frac{r^2}{\beta_i^2}}, \quad V_\tau(r) = \sum_{i=1}^3 \alpha_i^{(\tau)} e^{-\frac{r^2}{\beta_i^2}} \\ V_{\sigma\tau}(r) &= \sum_{i=1}^3 \alpha_i^{(\sigma\tau)} e^{-\frac{r^2}{\beta_i^2}} + \lambda_1^{(\sigma\tau)} \mathcal{Y}(\rho_1, m_\pi, r). \end{aligned} \quad (11)$$

The relation between the parameters are imposed as

$$\begin{pmatrix} \alpha_i(^{11}S_0) \\ \alpha_i(^{31}S_0) \\ \alpha_i(^{13}S_1) \\ \alpha_i(^{33}S_1) \end{pmatrix} = \hat{A} \begin{pmatrix} \alpha_i^{(0)} \\ \alpha_i^{(\sigma)} \\ \alpha_i^{(\tau)} \\ \alpha_i^{(\sigma\tau)} \end{pmatrix}, \quad \begin{pmatrix} \lambda_1(^{11}S_0) \\ \lambda_1(^{31}S_0) \\ \lambda_1(^{13}S_1) \\ \lambda_1(^{33}S_1) \end{pmatrix} = \begin{pmatrix} 9\lambda_1^{(\sigma\tau)} \\ -3\lambda_1^{(\sigma\tau)} \\ -3\lambda_1^{(\sigma\tau)} \\ \lambda_1^{(\sigma\tau)} \end{pmatrix}, \quad (12)$$

and $\lambda_2(C) = \lambda_2^{(0)}$ being independent of the channel, C .

It is in order here to mention about the fitting procedure of the off-diagonal $\Lambda\Lambda$ - $N\Xi$ potential. Although there is nothing wrong to solve the coupled-channel Schrödinger equation with non-Hermitian potential, it is customary to use Hermitian potential in phenomenological studies in nuclear physics. Since the difference between $V_{N\Xi}^{\Lambda\Lambda}$ and $V_{\Lambda\Lambda}^{N\Xi}$ are confined only at short distances if any (see Fig. 1 (b,c)), it does not affect the low-energy scattering observables. We have checked this explicitly by choosing an Hermitian potential with the off-diagonal part is taken either $V_{N\Xi}^{\Lambda\Lambda}$, $V_{\Lambda\Lambda}^{N\Xi}$ or their average $\bar{V}_{N\Xi}^{\Lambda\Lambda} = (V_{N\Xi}^{\Lambda\Lambda} + V_{\Lambda\Lambda}^{N\Xi})/2$. As shown in Appendix B, the phase shifts in these three cases do not have difference within the statistical errors. Therefore, in the following we show the fit parameters corresponding to $\bar{V}_{N\Xi}^{\Lambda\Lambda}$.

Final fit parameters are given in Table 2 for $V^{\Lambda\Lambda}(^{11}S_0)$ and Table 3 for $\bar{V}_{N\Xi}^{\Lambda\Lambda}(^{11}S_0)$, with three different values $t/a = 11, 12, 13$. Also shown in Table 4 are those for $V^{N\Xi}$ in $^{11}S_0$, $^{31}S_0$, $^{13}S_1$ and $^{33}S_1$ channels with $t/a = 11, 12, 13$, where the data in all $N\Xi$ channels are fitted simultaneously. We perform uncorrelated fit for the potential, where the fit range is taken to be $r = [0, 2]$ fm independent of the potentials so that there are 220 coordinate data points to be fitted in each channel. For convenience, we show the corresponding parameters for $V^{N\Xi}$ in the operator basis in Table C.1. As for the choice of these t/a , see Appendix A.

Table 2: Fitted parameters for $V^{\Lambda\Lambda}(^{11}S_0)$ with statistical errors using the data for $r = [0, 2]\text{fm}$. α_i , β_i and ρ_i are given in units of [MeV], [fm] and [fm], respectively. λ_1 and λ_2 are given in units of [MeV · fm] and [MeV · fm²], respectively. The values of $\chi^2/\text{d.o.f.}$ with #d.o.f = 214 are 1.30(40), 0.76(18) and 0.74(30) for $t/a = 11, 12$ and 13 , respectively.

t/a	Gauss-1		Gauss-2		[Yukawa] ²	
	$\alpha_1^{\Lambda\Lambda}$	$\beta_1^{\Lambda\Lambda}$	$\alpha_2^{\Lambda\Lambda}$	$\beta_2^{\Lambda\Lambda}$	$\lambda_2^{\Lambda\Lambda}$	$\rho_2^{\Lambda\Lambda}$
11	1466.4(28.4)	0.160(5)	407.1(43.9)	0.366(18)	-170.3(32.2)	0.918(87)
12	1486.7(46.5)	0.156(7)	418.2(64.6)	0.367(25)	-160.0(50.8)	0.929(148)
13	1338.0(89.5)	0.143(10)	560.7(124.2)	0.322(27)	-176.2(114.9)	1.033(292)

Table 3: Fitted parameters for the transition potential $\bar{V}_{N\Xi}^{\Lambda\Lambda}(^{11}S_0)$ with the statistical errors using the data for $r = [0, 2]\text{fm}$. Units are the same as those in Table 2. The values of $\chi^2/\text{d.o.f.}$ with #d.o.f = 214 are 1.24(35), 1.01(28) and 1.13(28) for $t/a = 11, 12$ and 13 , respectively.

t/a	Gauss-1		Gauss-2		Yukawa	
	α_1	β_1	α_2	β_2	λ_1	ρ_1
11	1228.0(21.9)	0.187(7)	294.9(16.6)	0.433(16)	-69.7(16.2)	0.130(8)
12	1206.7(27.0)	0.191(12)	307.4(30.3)	0.438(25)	-75.2(26.9)	0.133(13)
13	1252.7(47.6)	0.187(25)	306.9(46.4)	0.428(58)	-65.8(58.1)	0.128(28)

The analytic forms of the potential, Eqs. (7), (8) and (10), together with the parameters in Table 2-4 are useful for phenomenological applications such as the calculation of the scattering phase shifts (as given in Fig. 4 and Fig. 5) and also the calculation of the binding energy of Ξ hypernuclei (as discussed in ref.[31]). The diagonal potentials (Fig.1(a), Fig.1(d) and Fig.2) are composed of the short-range part (parametrized by α_i and β_i) and the medium/long range part (parametrized by λ_i , ρ_i). The positive values of α_i correspond to short-range repulsion, while the negative values of λ_i correspond to medium/long range attraction.

6. Scattering observables

The $\Lambda\Lambda$ and $N\Xi$ coupled-channel scattering phase shifts in the $^{11}S_0$ channel are calculated by solving the coupled-channel Schrödinger equation in the infinite volume with the fitted potentials given in the previous section. Since we consider low-energy scatterings, we adopt the non-relativistic kinematics hereafter.

The $\Lambda\Lambda$ phase shifts and the inelasticity are defined by the $\Lambda\Lambda$ -component of the two-by-two S-matrix, $(\mathbf{S})_{\Lambda\Lambda} = \eta \exp(2i\delta_{\Lambda\Lambda})$. In Fig. 4 (a,b), they are shown as a function of the center-of-mass energy $E_{\text{CM}} = k^2/m_\Lambda$ with k being the relative momentum between Λ s for $t/a = 11, 12, 13$. The t -dependence is minor within the statistical errors. We found that $\Lambda\Lambda$ attraction is rather weak, as inferred from Fig. 1 (a). Accordingly, no bound or resonant di-hyperon exists around the $\Lambda\Lambda$ threshold in (2+1)-flavor QCD at nearly physical quark masses. This is in contrast to the case of a possible H -dibaryon in 3-flavor QCD at heavy quark masses [29, 30].

Low-energy part of $\Lambda\Lambda$ phase shifts in Fig. 4 (a) provides the scattering length and

Table 4: Fitted parameters for $V^{N\Xi}$ ($^{11}S_0, ^{31}S_0, ^{13}S_1, ^{33}S_1$) with the statistical errors using the data for $r = [0, 2]$ fm. In the last column, $\lambda_2(C)$ is independent of the channel, C . Units are the same as those in Table 2. For the corresponding parameters in the operator basis, see Table C.1. The values of $\chi^2/\text{d.o.f.}$ with $\#\text{d.o.f.} = 861$ are 2.34(39), 1.38(21) and 1.28(18) for $t/a = 11, 12$ and 13 , respectively.

$t/a = 11$	Gauss-1	Gauss-2	Gauss-3	Yukawa	[Yukawa] ²
	α_1	α_2	α_3	λ_1	λ_2
$^{11}S_0$	40.2(36.1)	51.5(28.2)	30.5(14.9)	-14.6(1.6)	-109.8(7.9)
$^{31}S_0$	1766.1(75.6)	920.3(56.8)	240.5(31.1)	4.9(5)	-109.8(7.9)
$^{13}S_1$	493.3(30.9)	300.8(22.9)	92.0(17.3)	4.9(5)	-109.8(7.9)
$^{33}S_1$	944.8(46.8)	568.6(29.8)	190.3(25.0)	-1.6(2)	-109.8(7.9)
	β_1	β_2	β_3	ρ_1	ρ_2
	0.129(3)	0.258(12)	0.569(21)	0.249(38)	0.609(23)

$t/a = 12$	Gauss-1	Gauss-2	Gauss-3	Yukawa	[Yukawa] ²
	α_1	α_2	α_3	λ_1	λ_2
$^{11}S_0$	-81.3(54.3)	171.1(59.1)	4.9(27.3)	-12.8(2.2)	-97.3(9.6)
$^{31}S_0$	1677.2(90.1)	991.3(62.7)	290.8(43.2)	4.3(7)	-97.3(9.6)
$^{13}S_1$	449.2(52.5)	348.9(31.8)	110.3(22.3)	4.3(7)	-97.3(9.6)
$^{33}S_1$	849.5(53.4)	653.9(32.7)	210.8(35.9)	-1.4(2)	-97.3(9.6)
	β_1	β_2	β_3	ρ_1	ρ_2
	0.124(3)	0.241(12)	0.533(22)	0.136(22)	0.603(48)

$t/a = 13$	Gauss-1	Gauss-2	Gauss-3	Yukawa	[Yukawa] ²
	α_1	α_2	α_3	λ_1	λ_2
$^{11}S_0$	62.4(125.4)	-43.6(144.7)	123.8(110.2)	-12.5(2.4)	-83.5(14.6)
$^{31}S_0$	1599.4(308.3)	879.8(324.3)	496.7(136.8)	4.2(8)	-83.5(14.6)
$^{13}S_1$	345.5(106.5)	287.0(153.7)	268.9(120.9)	4.2(8)	-83.5(14.6)
$^{33}S_1$	836.0(163.3)	487.2(213.1)	383.1(125.2)	-1.4(3)	-83.5(14.6)
	β_1	β_2	β_3	ρ_1	ρ_2
	0.124(10)	0.228(34)	0.499(33)	0.307(307)	0.417(74)

the effective range using the S -wave effective range expansion (ERE) formula,

$$k \cot \delta = -\frac{1}{a_0} + \frac{1}{2}r_{\text{eff}}k^2 + \mathcal{O}(k^4), \quad (13)$$

where we use the sign convention of a_0 in nuclear and atomic physics. The results are

$$a_0^{(\Lambda\Lambda)} = -0.81 \pm 0.23_{-0.13}^{+0.00} \text{ [fm]}, \quad r_{\text{eff}}^{(\Lambda\Lambda)} = 5.47 \pm 0.78_{-0.55}^{+0.09} \text{ [fm]}, \quad (14)$$

where the central values and the statistical errors are estimated at $t/a = 12$, while the systematic errors are estimated from the central values for $t/a = 11$ and 13 . For comparison, the experimental neutron-neutron ERE parameters are $(a_0^{(nn)}, r_{\text{eff}}^{(nn)}) = (-18.5, 2.80)$ fm. Our results in Eq. (14) were recently confirmed to be consistent with a constraint obtained from the $\Lambda\Lambda$ momentum correlation of in p-p and p-Pb collisions [8]. (Note that the sign convention of a_0 in [8] is defined to be opposite from ours.)

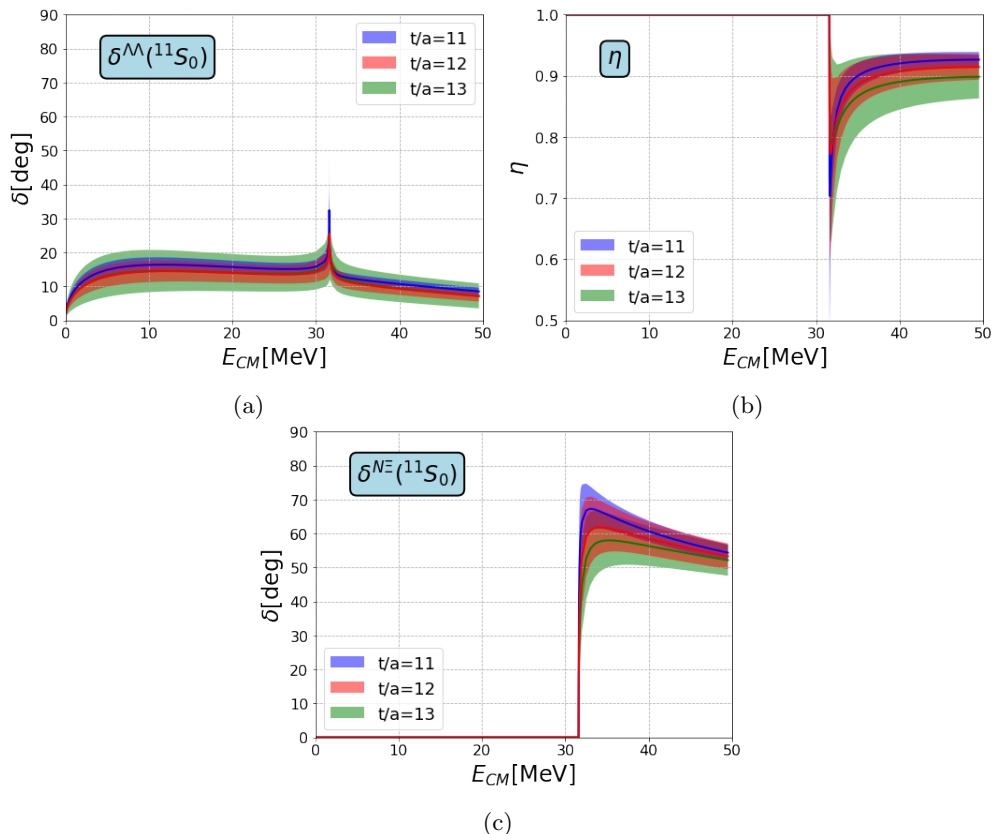


Figure 4: (a) $\Lambda\Lambda$ scattering phase shift, (b) $\Lambda\Lambda$ inelasticity, and (c) $N\Xi$ scattering phase shift in the $^{11}S_0$ channel.

We note that the $\Lambda\Lambda$ phase shift in Fig. 4 (a) and the inelasticity η in Fig. 4 (b) near the $N\Xi$ threshold, show a sharp enhancement and a rapid drop and show an enhancement, respectively, due to the off-diagonal coupling. Also, Fig. 4 (c) shows a sharp increase of the $N\Xi$ phase shift $\delta^{N\Xi}$ up to about 60° just above the $N\Xi$ threshold, which indicates a significant $N\Xi$ attraction in the $^{11}S_0$ channel. Indeed, we have confirmed that the $N\Xi$ system is in the unitary region and a virtual pole is created in the $^{11}S_0$ channel.

The S -wave $N\Xi$ scattering phase shifts in $^{31}S_0$, $^{13}S_1$ and $^{33}S_1$ channel are shown in Fig. 5 as a function of $E_{\text{CM}} = k^2 \times (1/(2m_N) + 1/(2m_\Xi))$. We find that the interaction in the $^{31}S_0$ channel is weakly repulsive while the $^{13}S_1$ and $^{33}S_1$ channels are weakly attractive, at low energies.

7. Summary and conclusion remarks

We have studied strangeness $S = -2$ baryon-baryon interactions focusing on the S -wave $\Lambda\Lambda$ and $N\Xi$ potentials using the (2+1)-flavor lattice QCD configurations at the almost physical point ($m_\pi \simeq 146\text{MeV}$ and $m_K \simeq 525\text{MeV}$) analyzed by the coupled-channel HAL QCD method. Resultant lattice QCD potentials in different isospin-spin channels ($^{11}S_0$, $^{31}S_0$, $^{13}S_1$ and $^{33}S_1$) are parametrized by analytic functions (a combination of Gaussian and Yukawa forms) for calculating the scattering observables such as the phase shift and inelasticity.

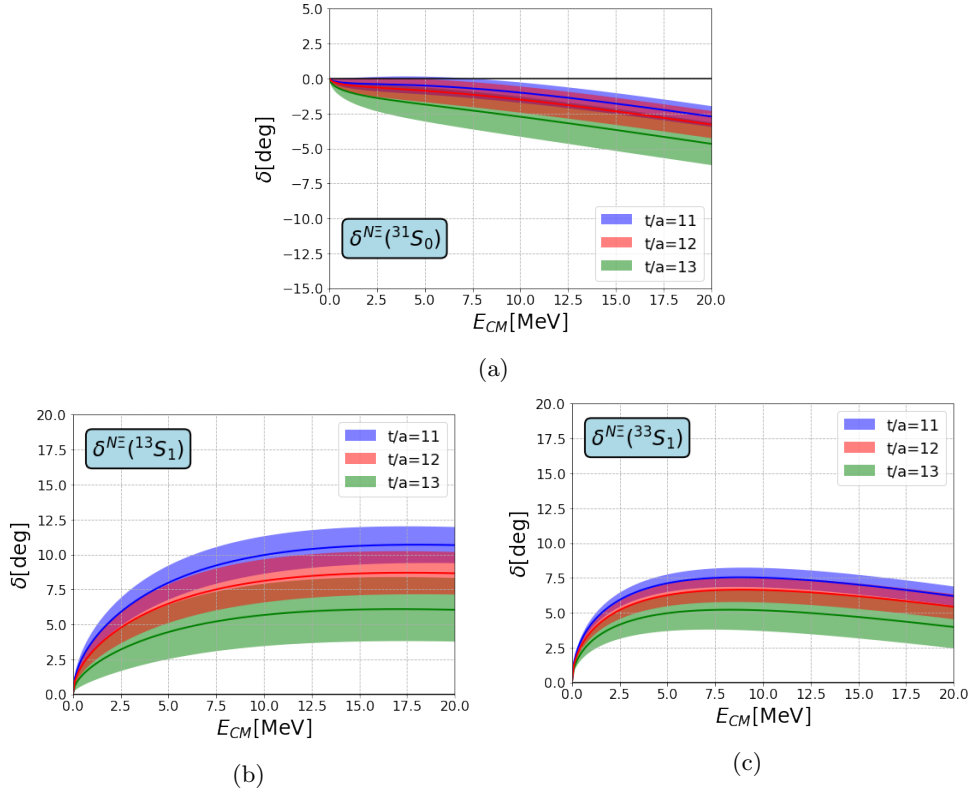


Figure 5: The $N\Xi$ scattering phase shifts in ${}^{31}S_0$, ${}^{13}S_1$ and ${}^{33}S_1$ are shown in (a), (b) and (c), respectively.

We found that $\Lambda\Lambda$ (${}^{11}S_0$) has attraction at low-energies, while it is not strong enough to generate bound or resonant dihyperon around the $\Lambda\Lambda$ threshold. Our scattering length and the effective range in Eq. (14) were recently confirmed to be consistent with an experimental constraint by ALICE experiment at LHC [8]. On the other hand, we found that the $N\Xi$ (${}^{11}S_0$) has relatively a strong attraction to drive the system into the unitary regime, while $N\Xi$ (${}^{31}S_0$) is weakly repulsive and $N\Xi$ (${}^{13}S_1$) and $N\Xi$ (${}^{33}S_1$) are weakly attractive. These features may lead to a light Ξ hypernuclei as recently discussed in [31]. Also, they introduce an attractive momentum correlation between proton and Ξ^- on top of the Coulomb attraction as suggested in [32] and confirmed recently by ALICE experiment at LHC [9].

There remain several future problems to be solved. First of all, we need to carry out (2+1)-flavor and (1+1+1)-flavor lattice simulations exactly at the physical point to check whether the virtual pole in the $N\Xi$ (${}^{11}S_0$) channel turns into a resonance below the $N\Xi$ threshold. Another issue is to carry out full channel coupling analysis with $\Lambda\Sigma$ and $\Sigma\Sigma$ to cover the scattering energy beyond the $\Lambda\Sigma$ threshold.

Acknowledgements

We thank members of PACS Collaboration for the gauge configuration generations. The lattice QCD calculations have been performed on the K computer at RIKEN (hp120281,

hp130023, hp140209, hp150223, hp150262, hp160211, hp170230), HOKUSAI FX100 computer at RIKEN (G15023, G16030, G17002) and HA-PACS at University of Tsukuba (14a-20, 15a-30). We thank ILDG/JLDG [33, 34, 35] which serves as an essential infrastructure in this study. We thank the authors of cuLGT code [36] for the gauge fixing. This work is supported in part by the Grant-in-Aid of the Japanese Ministry of Education, Sciences and Technology, Sports and Culture (MEXT) for Scientific Research (Nos. JP16H03978, JP18H05236, JP18H05407, JP19K03879), by SPIRE (Strategic Program for Innovative REsearch), by Priority Issue on Post-K computer (Elucidation of the Fundamental Laws and Evolution of the Universe) and by Joint Institute for Computational Fundamental Science (JICFuS).

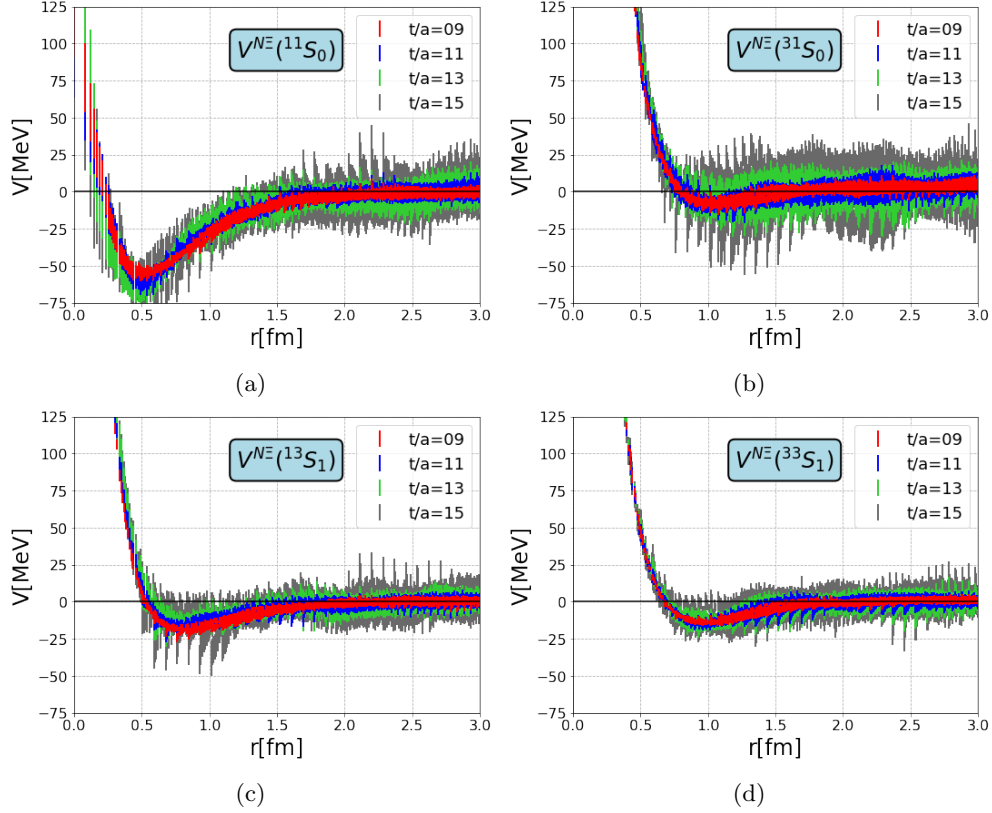


Figure A.1: The t -dependence of S -wave $N\Xi$ potentials. The $V^{N\Xi}(^{11}S_0)$, $V^{N\Xi}(^{31}S_0)$, $V^{N\Xi}(^{13}S_1)$ and $V^{N\Xi}(^{33}S_1)$ are shown in (a), (b), (c) and (d), respectively.

Appendix A. t -dependence of $N\Xi$ potentials

Fig. A.1 shows the t -dependence of S -wave $N\Xi$ potentials in the range $t/a = 9$ to 15 which is wider than that used in the text. Overall stability of the results in this wider range of t/a can be seen within the statistical error bars. Nevertheless, we find that the fitting by analytic functions in Sec. 5 is rather unstable against at short time (e.g. $t/a \leq 10$) probably due to the inelastic state contaminations. Also the large statistical errors prevent us to extract sensible fit parameters for $t/a \geq 14$. This is why we chose the optimal range $11 \leq t/a \leq 13$ throughout this paper.

Appendix B. Dependence on different off-diagonal potentials

To check the observable difference among three choices of the off-diagonal part of the Hermitian potential ($V_{N\Xi}^{\Lambda\Lambda}$, $V_{\Lambda\Lambda}^{N\Xi}$ and their average $\bar{V}_{N\Xi}^{\Lambda\Lambda}$), the $\Lambda\Lambda$ scattering phase shifts and the $N\Xi$ scattering phase shifts are shown in Fig. B.1 and in Fig. B.2, respectively. Within the statistical errors, three results are consistent with each other for all t/a used in this paper. Thus we consider $\bar{V}_{N\Xi}^{\Lambda\Lambda}$ in the text.

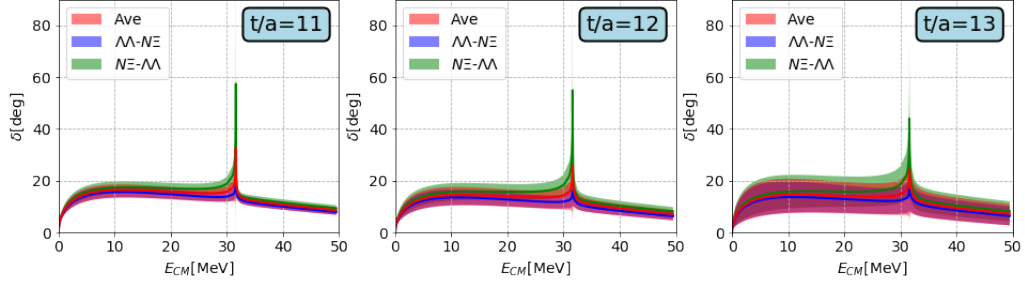


Figure B.1: The $\Lambda\Lambda$ scattering phase shifts for $t/a = 11$ (left), $t/a = 12$ (middle) and $t/a = 13$ (right). Blue, green and red curves correspond to the phase shifts calculated with $V_{N\Xi}^{\Lambda\Lambda}$, $V_{\Lambda\Lambda}^{N\Xi}$ and $\bar{V}_{N\Xi}^{\Lambda\Lambda}$, respectively.

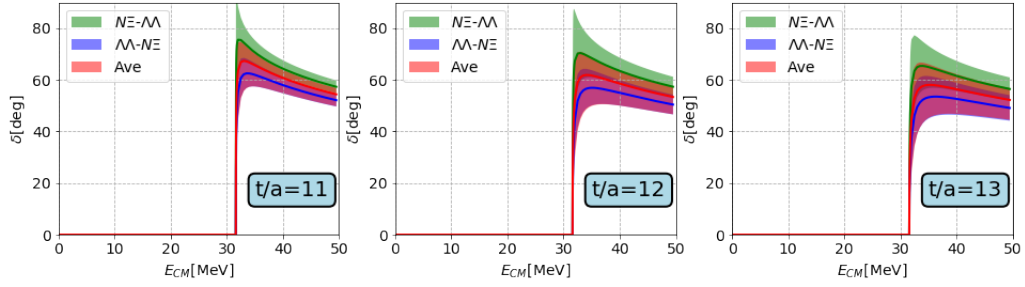


Figure B.2: Same with Fig. B.1 but for $N\Xi$ scattering phase shifts.

Appendix C. Fit parameters of $N\Xi$ potentials in the operator basis

We show the fit parameters of $N\Xi$ potentials in the operator basis, $(V_0, V_\sigma, V_\tau, V_{\sigma\tau})$ given in Eq. (5). For parameters in the spin-isospin basis, see Table 4.

Table C.1: Fitting parameters for $V^{N\Xi}$ in the operator basis with the statistical errors. Units are the same as those in Table 4.

$t/a = 11$	Gauss-1 α_1	Gauss-2 α_2	Gauss-3 α_3	Yukawa λ_1	$[\text{Yukawa}]^2$ λ_2
V_0	957.6(44.7)	552.0(29.3)	171.3(23.6)	—	-109.8(7.9)
V_σ	-125.7(8.3)	-50.4(6.5)	-5.6(1.6)	—	—
V_τ	192.5(9.9)	104.5(8.0)	31.6(3.1)	—	—
$V_{\sigma\tau}$	-79.6(2.7)	-37.6(2.8)	-7.0(0.9)	-1.6(2)	—
	β_1	β_2	β_3	ρ_1	ρ_2
	0.129(3)	0.258(12)	0.569(21)	0.249(38)	0.609(23)

$t/a = 12$	Gauss-1 α_1	Gauss-2 α_2	Gauss-3 α_3	Yukawa λ_1	$[\text{Yukawa}]^2$ λ_2
V_0	871.4(54.6)	629.8(33.0)	194.1(33.0)	—	-97.3(9.6)
V_σ	-122.0(9.3)	-52.2(8.9)	-8.4(2.7)	—	—
V_τ	185.0(10.0)	108.5(7.2)	36.7(5.2)	—	—
$V_{\sigma\tau}$	-84.9(5.7)	-32.2(5.4)	-11.6(1.6)	-1.4(2)	—
	β_1	β_2	β_3	ρ_1	ρ_2
	0.124(3)	0.241(12)	0.533(22)	0.136(22)	0.603(48)

$t/a = 13$	Gauss-1 α_1	Gauss-2 α_2	Gauss-3 α_3	Yukawa λ_1	$[\text{Yukawa}]^2$ λ_2
V_0	838.9(158.0)	490.1(206.4)	366.8(123.9)	—	-83.5(14.6)
V_σ	-125.4(27.1)	-53.0(24.1)	-12.2(4.4)	—	—
V_τ	188.0(40.5)	95.2(36.6)	44.7(8.4)	—	—
$V_{\sigma\tau}$	-65.4(20.6)	-45.2(17.2)	-16.2(4.7)	-1.4(3)	—
	β_1	β_2	β_3	ρ_1	ρ_2
	0.124(10)	0.228(34)	0.499(33)	0.307(307)	0.417(74)

References

- [1] R. L. Jaffe, Phys. Rev. Lett. **38** (1977) 195 [Erratum-ibid. **38** (1977) 617].
- [2] T. Sakai, K. Shimizu and K. Yazaki, Prog. Theor. Phys. Suppl. **137** (2000) 121 [nucl-th/9912063].
- [3] B. H. Kim *et al.* [Belle Collaboration], Phys. Rev. Lett. **110** (2013) 222002 [arXiv:1302.4028 [hep-ex]].
- [4] K. Nakazawa *et al.*, PTEP **2015** (2015) 033D02.
- [5] A. Gal, E. V. Hungerford, and D. J. Millener, Rev. Mod. Phys. **88** (2016) 035004.
- [6] E. Hiyama and K. Nakazawa, Ann. Rev. Nucl. Part. Sci. **68** (2018) 131.
- [7] Adamczyk *et al.* [STAR collaboration], Phys. Rev. Lett. **114** (2015) 022301.
- [8] S. Acharya *et al.* [ALICE Collaboration], Phys. Rev. C **99**, 024001 (2019) [arXiv:1805.12455 [nucl-ex]]; Phys. Lett. B **797**, 134822 (2019) [arXiv:1905.07209 [nucl-ex]].
- [9] S. Acharya *et al.* [ALICE Collaboration], Phys. Rev. Lett. **123** (2019) 112002 [arXiv:1904.12198 [nucl-ex]].
- [10] N. Ishii, S. Aoki and T. Hatsuda, Phys. Rev. Lett. **99** (2007) 022001 [nucl-th/0611096].
- [11] S. Aoki, T. Hatsuda and N. Ishii, Prog. Theor. Phys. **123** (2010) 89 [arXiv:0909.5585 [hep-lat]].
- [12] N. Ishii *et al.* [HAL QCD Collaboration], Phys. Lett. B **712** (2012) 437 [arXiv:1203.3642 [hep-lat]].
- [13] S. Aoki *et al.* [HAL QCD Collaboration], Proc. Japan Acad. B **87** (2011) 509 [arXiv:1106.2281 [hep-lat]].

- [14] S. Aoki, B. Charron, T. Doi, T. Hatsuda, T. Inoue and N. Ishii, Phys. Rev. D **87** (2013) 034512 [arXiv:1212.4896 [hep-lat]].
- [15] K. Sasaki *et al.* [HAL QCD Collaboration], PTEP **2015** (2015) 113B01 [arXiv:1504.01717 [hep-lat]].
- [16] T. Iritani *et al.* [HAL QCD Collaboration], Phys. Lett. B **792** (2019) 284 [arXiv:1810.03416 [hep-lat]].
- [17] S. Gongyo *et al.*, Phys. Rev. Lett. **120** (2018) 212001 [arXiv:1709.00654 [hep-lat]].
- [18] T. Iritani *et al.* [HAL QCD Collaboration], Phys. Rev. D **99** (2019) 014514 [arXiv:1805.02365 [hep-lat]].
- [19] T. Iritani *et al.* [HAL QCD Collaboration], JHEP **1903** (2019) 007 [arXiv:1812.08539 [hep-lat]].
- [20] K.-I. Ishikawa *et al.* [PACS Collaboration], PoS LATTICE **2015** (2016) 075 [arXiv:1511.09222 [hep-lat]].
- [21] K. I. Ishikawa *et al.* [PACS Collaboration], Phys. Rev. D **98** (2018) 074510 [arXiv:1807.03974 [hep-lat]].
- [22] T. Boku *et al.*, PoS LATTICE **2012** (2012) 188 [arXiv:1210.7398 [hep-lat]].
- [23] M. Terai, K. I. Ishikawa, Y. Sugisaki, K. Minami, F. Shoji, Y. Nakamura, Y. Kuramashi, M. Yokokawa, IPSJ Transactions on Advanced Computing Systems, Vol.6 No.3 43-57 (Sep. 2013) (in Japanese).
- [24] Y. Nakamura, K.-I. Ishikawa, Y. Kuramashi, T. Sakurai and H. Tadano, Comput. Phys. Commun. **183** (2012) 34 [arXiv:1104.0737 [hep-lat]].
- [25] Y. Osaki and K. I. Ishikawa, PoS LATTICE **2010** (2010) 036 [arXiv:1011.3318 [hep-lat]].
- [26] T. Doi and M. G. Endres, Comput. Phys. Commun. **184** (2013) 117 [arXiv:1205.0585 [hep-lat]].
- [27] H. Nemura, Comput. Phys. Commun. **207** (2016) 91 [arXiv:1510.00903 [hep-lat]].
- [28] S. Okubo and R. E. Marshak, Ann. of Phys. **4** (1958)166.
- [29] T. Inoue *et al.* [HAL QCD Collaboration],
 Prog. Theor. Phys. **124** (2010) 591 [arXiv:1007.3559 [hep-lat]];
 Phys. Rev. Lett. **106** (2011) 162002 [arXiv:1012.5928 [hep-lat]];
 Nucl. Phys. A **881** (2012) 28 [arXiv:1112.5926 [hep-lat]].
- [30] S. R. Beane *et al.* [NPLQCD Collaboration], Phys. Rev. Lett. **106** (2011) 162001 [arXiv:1012.3812 [hep-lat]].
- [31] E. Hiyama, K. Sasaki, T. Miyamoto, T. Doi, T. Hatsuda, Y. Yamamoto and T. A. Rijken, Phys. Rev. Lett. **124** (2020) no.9, 092501 [arXiv:1910.02864 [nucl-th]].
- [32] T. Hatsuda, K. Morita, A. Ohnishi and K. Sasaki, Nucl. Phys. A **967** (2017) 856 [arXiv:1704.05225 [nucl-th]].
- [33] International Lattice Data Grid (ILDG), (Available at:<http://plone.jldg.org/>).
- [34] Japan Lattice Data Grid (JLDG), (Available at:<http://www.jldg.org/>).
- [35] T. Amagasa, *et al.*, J. Phys. Conf. Ser. **664** (2015) 042058.
- [36] M. Schröck and H. Vogt, Comput. Phys. Commun. **184** (2013) 1907 [arXiv:1212.5221 [hep-lat]].